ELSEVIER

International Journal of Solids and Structures 41 (2004) 1377–1393

INTERNATIONAL JOURNAL OF SOLIDS and STRUCTURES

www.elsevier.com/locate/ijsolstr

Three-dimensional stress analysis of textile composites: Part I. Numerical analysis

Sangwook Sihn [a,*], Endel V. Iarve [a], Ajit K. Roy [b]

[a] *Nonmetallic Division, University of Dayton Research Institute, 300 College Park, Dayton, OH 45469-0168, USA*
[b] *Air Force Research Laboratory, Materials and Manufacturing Directorate, AFRL/MLBC, 2941 P St Rm. 136, WPAFB, OH 45433-7750, USA*

Received 2 June 2003; received in revised form 14 October 2003

Abstract

Three-dimensional stress analysis in a unit-cell of a plain-woven composite was performed by using B-spline displacement approximation. The spline approximation provides continuity of displacement and stress components within each yarn and matrix subregion. Two types of unit-cell problems with and without inter-yarn delamination were considered. A penalty function approach along with a contact surface characteristic function was used to obtain a full-field numerical solution for the frictionless contact problem between delaminated yarn surfaces.

Yarn interfaces at yarn-crossover locations represent three-material wedge-type regions resulting in singular stress behavior. In the case of unit-cells with perfect bonding between the yarn interfaces, the numerical values of the inter-yarn normal stress did not exhibit trends typical for unbounded stress behavior, whereas the inter-yarn shear stress components displayed discontinuous behavior typical for numerical results in the vicinity of the stress singularity. In the presence of the delamination, both the inter-yarn normal and shear stress components exhibited unbounded behavior near the singularity. Notably, the inter-yarn normal stress showed signs of singular behavior in both cases of open and closed delaminations. Due to the stress singularity that exists at yarn-crossover locations containing three materials (yarn–yarn–matrix) interface intersections, the full-field numerical solution, even with high-order approximation functions, was not able to capture the directional nonuniqueness of the stress values in the vicinity of the singularity, and therefore calls for incorporation of the asymptotic singular stress analysis, which will be given in a follow-on paper [Sihn and Roy, International Journal of Solids and Structures (accepted for publication)].

Keywords: Woven composites; B-spline approximation method; Inter-yarn stresses

1. Introduction

The innovative weaving and braiding process opens up new opportunities for manufacturing three-dimensional (3-D) textile (preformed) composite structures with significantly increased damage resistance/

* Corresponding author. Tel.: +1-937-2559324; fax: +1-937-2588075.
E-mail address: sangwook@stanfordalumni.org (S. Sihn).

0020-7683/$ - see front matter © 2003 Elsevier Ltd. All rights reserved.
doi:10.1016/j.ijsolstr.2003.10.017

tolerance and durability combined with design flexibility and near net-shape processing. The fiber tows in the textile preform can be selectively placed and integrally woven in preferred directions (especially in the thickness direction) to overcome the inherent weakness of low through-the-thickness damage tolerance and strength of traditional laminated composites. The 3-D textile preform has been found to significantly enhance the fatigue life of composite joints, due to its exceptional through-the-thickness strength.

However, unlike processing traditional laminated composites, the relative spatial locking of the reinforcing tows (yarns) due to 3-D intertwining of the tows (yarns) prevents free chemical shrinkage of resin during processing, and hence causes process-induced yarn interface and matrix cracks in polymer matrix textile composites, as shown in Fig. 1. Although 3-D textile composites offer tremendous potential, unless this cracking phenomenon of the 3-D textile composites is understood and the stability of these cracks (damage tolerance) under load is quantified, the designers lack confidence in transitioning the 3-D textile composites in real structures.

Furthermore, *in situ* experimental observation by Roy (1996) of damage initiation in two-dimensional (2-D) textile composites reveals that the damage initiates in the form of interface cracks in the vicinity of yarn crimping, which is strongly influenced by the inter-yarn stresses in the interface region. Therefore, in order to understand and quantify the cracking mechanism, and to determine damage tolerance and energy release rates, etc., one needs an accurate prediction of the stress field, especially the inter-yarn stresses, in the interface region as well as near the crack tip in the woven or textile composites.

Numerous research work on modeling of the textile composites has been performed based on a representative volume element or a representative unit-cell approach, and devoted to prediction of effective properties. Tan et al. (1997) reviewed 115 articles on the prediction of effective mechanical properties of the textile composites, and Bystrom et al. (2000) evaluated different model predictions and compared them with experimental data. Yang et al. (1986) derived a fiber inclination model for the calculation of the effective in-plane elastic properties. The model treated the unit-cell of the woven composites as an assemblage of inclined unidirectional laminates, which were solved by the classical laminated plate theory. Naik and Shembekar (1992), Shembekar and Naik (1992) and Naik and Ganesh (1992) developed 2-D models for the elastic analysis of the plain-woven composites by taking into account the actual cross-section geometry, gap between two adjacent yarns and undulation, and continuity of yarns along both the warp and fill directions. Naik and Ganesh (1994, 1996) developed a 2-D model for prediction of in-plane failure strength under in-plane shear and uniaxial tensile loadings, respectively.

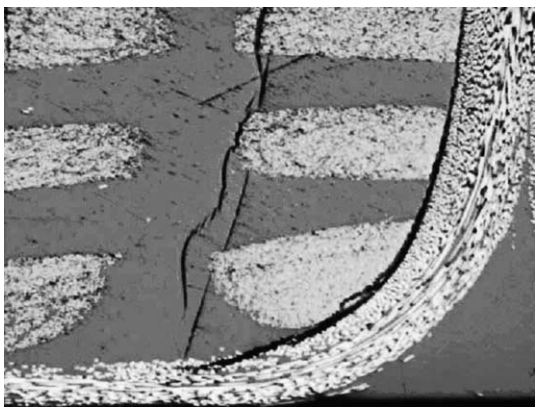

Fig. 1. Process-induced microcracking in three-dimensional textile (preform) composite.

Some analytical models oversimplify many architectural parameters in the woven composites, such as yarn undulation or fiber continuity, under an assumption of uniform stress and strain components in the crimp region. Because of the complex yarn architecture, numerical analyses, such as a finite element analysis, were preferred in the textile composite modeling. Most of the numerical models considered the yarns as separate homogeneous unidirectional materials with continuous yarn undulation. Whitcomb (1991) performed detailed 3-D finite element analysis of plain-woven composites, and illustrated the effects of tow waviness on composite moduli, Poisson's ratios and internal strain distributions. Woo and Whitcomb (1994, 1996) developed a practical computational procedure based on a global/local finite element method for the 3-D stress analysis of plain-woven composites. Woo and Whitcomb (2000) used post-processing with macroelements for calculating stresses of woven composites.

This level of analysis, which took into account the crimp and undulation of the yarns and their interaction with the matrix material, enabled researchers to perform failure analyses of the textile composites. Naik et al. (2002) performed stress and failure analysis of 3-D angle interlock woven composites under uniaxial static tensile and shear loadings. Drapier and Wisnom (1999) used the finite element method to investigate interlaminar shear behavior of non-crimp-fabric-based composites. It was established that the interlaminar shear behavior was controlled by the development of high shear-strain concentrations induced by the combination of mechanical and mesoscopic geometrical characteristics, and these shear-strain concentrations were more likely to lead to local damage.

However, to date, no special attention has been paid to the accuracy of the stress field predictions near the inter-yarn interface regions. Sihn and Roy (2001) analyzed the 3-D stress field of a unit-cell of a plain-woven composite by using a mixed finite element method. This work considered the fiber yarns as homogeneous unidirectional materials with continuously varying orientation and performed detailed stress analysis in the vicinity of the crimping regions. The result revealed a singular stress behavior in the interface region of the three-material (yarn crossover and matrix) junction. This singular stress field phenomenon at the junction of three-material discontinuity is similar to the singular stress field of the free-edge stress field of laminated composites. The numerical finite element analysis of using polynomial shape functions, as was used by Sihn and Roy (2001), even with higher order polynomials and extremely refined mesh failed to satisfy the interface stress continuity at the interface of the three-material junctions. Further, the mixed finite element formulation of Sihn and Roy (2001), due to a large number of variables involved, did not provide suitable computational efficiency. Therefore, it is desirable to ensure the validity of the stress calculation, the interfacial normal and shear stress components in particular, near the yarn-crossover location (three-material junction) with suitable computational efficiency.

In view of obtaining the accurate singular stress field with desirable computational efficiency, the present study is devoted to prediction of the singular stress fields in the inter-yarn interface regions by using a two-step approach. First, a numerical method based on a B-spline displacement approximation (Iarve, 1996) will be applied for 3-D stress analysis in the unit-cell of the plain-woven composites. Two configurations of the unit-cell with and without inter-yarn delamination will be considered, focusing on the validity of the interfacial stress components near the material junction. A contact algorithm was used to model the inter-yarn delamination in order to avoid yarn interpenetration. A penalty function approach along with contact surface characteristic functions was used to formulate the contact problem. The results of these analyses will be reported in the present paper.

Then we will perform an asymptotic analysis on the triple material junction (yarn-crossover location) and obtain powers of stress singularity for various yarn and matrix materials and crimp angles. The coefficients of the asymptotic expansion will be obtained by comparing the asymptotic solution with the full-field numerical solution in the vicinity of the material intersection region. This development will be reported in part II, an adjoining paper (Sihn et al., accepted for publication).

2. Problem statement

The unit-cell of the plain-woven composite was modeled by dividing it into several homogeneous subregions; each subregion was occupied by a characteristic fabric yarn or matrix, as shown in Fig. 2. Warp and fill yarns were defined as the yarns filled with fiber bundles aligned along the x- and y-directions, respectively, in a global xyz-coordinate system, while the remaining space in the unit-cell was filled with resin matrix material. Subregions 1 and 4 correspond to the warp yarns, subregions 2 and 3 to the fill yarns, and subregions 5 and 6 to the matrix material. The unit-cell of the plain-woven composites has dimensions of the lengths of warp and fill yarns, $L_w = L_f = 2.8575$ mm, and the half thicknesses of the yarns, $t_w = t_f = 0.142875$ mm, representing a typical plain-woven composite of 12K (12,000 carbon fibers in a tow) tows with tow spacing of 0.59 tows per mm (15 tows per inch).

Yarn waviness was assumed to be sinusoidal, and the functional forms of the lower and upper surfaces of subregions 1–6 in Fig. 2 can be written as follows:

$$
\begin{aligned}
z_L^{(1)} &= t_f\left(1-\cos\frac{\pi x}{L_w}\right)+t_w\left(1-\cos\frac{\pi y}{L_f}\right), & z_U^{(1)} &= t_f\left(1-\cos\frac{\pi x}{L_w}\right)+t_w\left(1+\cos\frac{\pi y}{L_f}\right),\\
z_L^{(2)} &= t_f\left(1+\cos\frac{\pi x}{L_w}\right)+t_w\left(1-\cos\frac{\pi y}{L_f}\right), & z_U^{(2)} &= t_f\left(1-\cos\frac{\pi x}{L_w}\right)+t_w\left(1-\cos\frac{\pi y}{L_f}\right),\\
z_L^{(3)} &= t_f\left(1-\cos\frac{\pi x}{L_w}\right)+t_w\left(1+\cos\frac{\pi y}{L_f}\right), & z_U^{(3)} &= t_f\left(1+\cos\frac{\pi x}{L_w}\right)+t_w\left(1+\cos\frac{\pi y}{L_f}\right),\\
z_L^{(4)} &= t_f\left(1+\cos\frac{\pi x}{L_w}\right)+t_w\left(1+\cos\frac{\pi y}{L_f}\right), & z_U^{(4)} &= t_f\left(1+\cos\frac{\pi x}{L_w}\right)+t_w\left(1-\cos\frac{\pi y}{L_f}\right),
\end{aligned}
\qquad (1)
$$

$$z_L^{(5)} = 0$$

and

$$
z_U^{(5)} = \begin{cases}
t_f\left(1-\cos\frac{\pi x}{L_w}\right)+t_w\left(1-\cos\frac{\pi y}{L_f}\right) & \text{for } 0\leqslant x\leqslant L_w/2,\ 0\leqslant y\leqslant L_f/2,\\
t_f\left(1+\cos\frac{\pi x}{L_w}\right)+t_w\left(1-\cos\frac{\pi y}{L_f}\right) & \text{for } L_w/2\leqslant x\leqslant L_w,\ 0\leqslant y\leqslant L_f/2,\\
t_f\left(1-\cos\frac{\pi x}{L_w}\right)+t_w\left(1+\cos\frac{\pi y}{L_f}\right) & \text{for } 0\leqslant x\leqslant L_w/2,\ L_y/2\leqslant y\leqslant L_f,\\
t_f\left(1+\cos\frac{\pi x}{L_w}\right)+t_w\left(1+\cos\frac{\pi y}{L_f}\right) & \text{for } L_w/2\leqslant x\leqslant L_w,\ L_y/2\leqslant y\leqslant L_f,
\end{cases}
\qquad (2)
$$

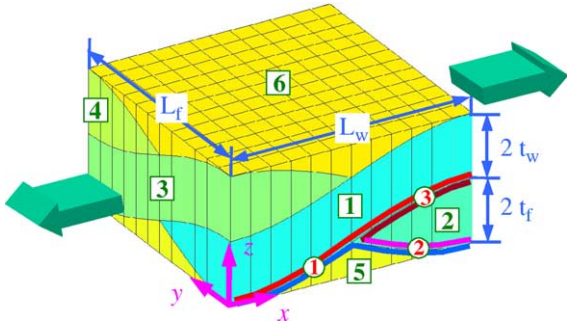

Fig. 2. A representative unit-cell of plain-woven composites, and geometric parameters describing the unit-cell. Numbers in boxes are subregion numbers, and numbers in circles are interface-line numbers. Interface line 1 is within $0\leqslant x\leqslant L_w/2$ and interface lines 2 and 3 are within $L_w/2\leqslant x\leqslant L_w$.

$$z_L^{(6)} = \begin{cases} t_f\left(1+\cos\frac{\pi x}{L_w}\right)+t_w\left(1+\cos\frac{\pi y}{L_f}\right) & \text{for } 0\leqslant x\leqslant L_w/2,\ 0\leqslant y\leqslant L_f/2, \\ t_f\left(1-\cos\frac{\pi x}{L_w}\right)+t_w\left(1+\cos\frac{\pi y}{L_f}\right) & \text{for } L_w/2\leqslant x\leqslant L_w,\ 0\leqslant y\leqslant L_f/2, \\ t_f\left(1+\cos\frac{\pi x}{L_w}\right)+t_w\left(1-\cos\frac{\pi y}{L_f}\right) & \text{for } 0\leqslant x\leqslant L_w/2,\ L_y/2\leqslant y\leqslant L_f, \\ t_f\left(1-\cos\frac{\pi x}{L_w}\right)+t_w\left(1-\cos\frac{\pi y}{L_f}\right) & \text{for } L_w/2\leqslant x\leqslant L_w,\ L_y/2\leqslant y\leqslant L_f, \end{cases}$$

and

$$z_U^{(6)} = 2(t_f + t_w), \tag{3}$$

where superscripts with parentheses indicate the subregion numbers, and subscripts L and U indicate the lower and upper surfaces, respectively.

The warp and fill yarns were modeled as transversely isotropic materials with its material symmetry axis aligned along the trajectory of the yarns. The transversely isotropic material properties of the yarns used in this study were as follows: longitudinal Young's modulus ($E_1 = 138$ GPa), transverse Young's modulus ($E_2 = E_3 = 10$ GPa), in-plane Poisson's ratio ($\nu_{12} = \nu_{13} = 0.3$), out-of-plane Poisson's ratio ($\nu_{23} = 0.5$), in-plane shear modulus ($G_{12} = G_{13} = 5.5$ GPa) and out-of-plane shear modulus ($G_{23} = 2.9$ GPa), representing the material properties of a unidirectional carbon fiber reinforced composite. The matrix was modeled as an isotropic material with $E_m = 3.75$ GPa and $\nu_m = 0.34$.

Two angles, yarn orientation angle θ_1 and crimp angle θ_2, were used to describe the yarn orientation with respect to global coordinates (xyz). The yarn orientation angle defined the projection of the fiber orientation in the yarn on the xy-plane with respect to the global x-axis. This angle is constant in each yarn and equal to 0° for the warp yarns and 90° for the fill yarns. The crimp angle was introduced for the local fiber-undulation directions in the xz-plane with respect to the x-axis for the warp yarns, and in the yz-plane with respect to the y-axis for the fill yarns. From Eq. (1), the crimp angle for the warp yarns (subregions 1 and 4) can be written as

$$\theta_2(x,y) = -\tan^{-1}\left(\frac{\partial z_U(x,y)}{\partial x}\right) \equiv -\tan^{-1}\left(\frac{\partial z_L(x,y)}{\partial x}\right), \tag{4}$$

and for the fill yarns (subregions 2 and 3) as

$$\theta_2(x,y) = \tan^{-1}\left(\frac{\partial z_U(x,y)}{\partial y}\right) \equiv \tan^{-1}\left(\frac{\partial z_L(x,y)}{\partial y}\right). \tag{5}$$

In all cases, since the tows are reinforced with unidirectional fibers, the crimp angle is a function of x and y only, so that it is considered as constant along the z-direction in each yarn, independent of z-direction within a tow (yarn).

Let an on-axis coordinate system represent directions of principal material axes in the yarns. In this coordinate system, the yarn stiffness matrix, $[C]_{on}$, is constant and corresponds to transversely isotropic material (Tsai, 1992). Let us denote the displacement, stress and strain components in the on-axis coordinates as $\{u\}_{on}$, $\{\sigma\}_{on}$ and $\{\varepsilon\}_{on}$, respectively. One can then express the displacement, stress and strain components in global xyz-coordinates ($\{u\}_{global}$, $\{\sigma\}_{global}$ and $\{\varepsilon\}_{global}$) as

$$\{u\}_{global} = [L_2(\theta_2)][L_1(\theta_1)]\{u\}_{on}, \tag{6}$$

$$\{\sigma\}_{global} = [T_2(\theta_2)][T_1(\theta_1)]\{\sigma\}_{on}, \tag{7}$$

$$\{\varepsilon\}_{global} = [T_2(\theta_2)]^{-T}[T_1(\theta_1)]^{-T}\{\varepsilon\}_{on}, \tag{8}$$

and the stiffness properties of the yarn in the global coordinate system ($[C]_{\text{global}}$) as

$$[C]_{\text{global}} = \{[T_2(\theta_2)][T_1(\theta_1)]\}[C]_{\text{on}}\{[T_2(\theta_2)][T_1(\theta_1)]\}^{\text{T}}, \tag{9}$$

where

$$[L_1(\theta_1)] = \begin{bmatrix} m_1 & -n_1 & 0 \\ n_1 & m_1 & 0 \\ 0 & 0 & 1 \end{bmatrix}, \tag{10}$$

$$[L_2(\theta_2)]^{\text{warp}} = \begin{bmatrix} m_2 & 0 & n_2 \\ 0 & 1 & 0 \\ -n_2 & 0 & m_2 \end{bmatrix} \quad \text{for the warp yarns,} \tag{11}$$

$$[L_2(\theta_2)]^{\text{fill}} = \begin{bmatrix} 1 & 0 & 0 \\ 0 & m_2 & -n_2 \\ 0 & n_2 & m_2 \end{bmatrix} \quad \text{for the fill yarns,} \tag{12}$$

$$[T_1(\theta_1)] = \begin{bmatrix} m_1^2 & n_1^2 & 0 & 0 & 0 & -2m_1n_1 \\ n_1^2 & m_1^2 & 0 & 0 & 0 & 2m_1n_1 \\ 0 & 0 & 1 & 0 & 0 & 0 \\ 0 & 0 & 0 & m_1 & n_1 & 0 \\ 0 & 0 & 0 & -n_1 & m_1 & 0 \\ m_1n_1 & -m_1n_1 & 0 & 0 & 0 & m_1^2 - n_1^2 \end{bmatrix}, \tag{13}$$

$$[T_2(\theta_2)]^{\text{warp}} = \begin{bmatrix} m_2^2 & 0 & n_2^2 & 0 & 2m_2n_2 & 0 \\ 0 & 1 & 0 & 0 & 0 & 0 \\ n_2^2 & 0 & m_2^2 & 0 & -2m_2n_2 & 0 \\ 0 & 0 & 0 & m_2 & 0 & -n_2 \\ -m_2n_2 & 0 & m_2n_2 & 0 & m_2^2 - n_2^2 & 0 \\ 0 & 0 & 0 & n_2 & 0 & m_2 \end{bmatrix} \quad \text{for the warp yarns,} \tag{14}$$

$$[T_2(\theta_2)]^{\text{fill}} = \begin{bmatrix} 1 & 0 & 0 & 0 & 0 & 0 \\ 0 & m_2^2 & n_2^2 & -2m_2n_2 & 0 & 0 \\ 0 & n_2^2 & m_2^2 & 2m_2n_2 & 0 & 0 \\ 0 & m_2n_2 & -m_2n_2 & m_2^2 - n_2^2 & 0 & 0 \\ 0 & 0 & 0 & 0 & m_2 & n_2 \\ 0 & 0 & 0 & 0 & -n_2 & m_2 \end{bmatrix} \quad \text{for the fill yarns,} \tag{15}$$

and $m_1 = \cos(\theta_1)$, $n_1 = \sin(\theta_1)$, $m_2 = \cos(\theta_2)$ and $n_2 = \sin(\theta_2)$.

The unit-cell was loaded with a constant displacement (u_o) in the x-direction under the following boundary conditions:

$$\begin{aligned} &u_x(0, y, z) = 0, \qquad u_x(L_{\text{w}}, y, z) = u_o, \\ &u_y(x, 0, z) = u_y(x, L_{\text{f}}, z) = u_z(x, y, 0) = 0. \end{aligned} \tag{16}$$

The numbers of subdivision intervals in each subvolume in the x- and y-directions were denoted as n_x and n_y, respectively, whereas those in the z-direction as n_z. Note that the length in the x-, y- and z-directions were $L_{\text{w}}/2$, $L_{\text{f}}/2$ and $2t_{\text{w}}$ and $2t_{\text{f}}$, respectively. Three different mesh schemes were used for the convergence study as follows:

1. Mesh #1: Uniform mesh with $n_x = n_y = 5$, $n_z = 2$.
2. Mesh #2: Uniform mesh with $n_x = n_y = 10$, $n_z = 4$.
3. Mesh #3: Nonuniform mesh with $n_x = n_y = 10$, $n_z = 4$, $q = 2$.

Nonuniform mesh was used to concentrate the subdivisions to particular points, especially at the yarn intersections. For example, $q = 2$ in the z-direction means that the size of the mesh at the interfacial surface of the yarns was two times smaller than that in the middle of the yarns. The stress results were normalized by an arbitrarily chosen factor of $\sigma_o = 0.01$ GPa.

3. Full-field numerical calculation

The full-field 3-D solution for the woven fabric composites is obtained based on the B-spline displacement approximation method implemented into a computer software, BSAM (2003).

3.1. B-spline approximation in a unit volume

Consider an elementary volume $[0,1]^3$ and a set of piecewise polynomial 3-D functions, $X_i(\mathbf{x})$, which provide a partition of unity-type basis functions for displacement approximation, so that

$$\mathbf{u}(\mathbf{x}) = \sum_i X_i(\mathbf{x})\mathbf{U}_i, \tag{17}$$

where $\mathbf{U}_i$ are displacement approximation coefficients, not necessarily associated with nodal displacements. The index, i, in Eq. (17) varies from 1 to the total number of approximation functions, which we will denote as a set Ω. 3-D shape functions $X_i(\mathbf{x})$ are constructed from one-dimensional sets of B-spline basis functions of order n and defect k as standard tensor products (Iarve, 1996, 1997).

Practical usefulness of the spline approximation for solution of boundary value problems is determined by the properties of the set of basis functions used in the analysis. The B-spline basis functions, possessing the shortest possible support for a given power n and defect k, represent an attractive computational efficiency (Iarve, 1996). The minimum support length property provides maximum sparsity of the resulting system of equations. Another significant advantage of the B-spline basis is the ability to change the defect of the spline at the end nodes. This allows one to build a system of basis functions such that the displacements at the end nodes are the actual coefficients of the spline functions. It provides a convenient way of imposing boundary conditions by simply assigning spline function coefficients analogous to the traditional finite element approximation. It should be noted that the displacements in the internal nodes are not explicitly equal to the coefficients of the B-spline functions.

A recurrent procedure based on polynomial representation (Iarve, 1996) is used to build the set of B-spline basis functions of arbitrary order and defect. Each one-dimensional basis spline function is non-negative and possesses a local support of no more than $n - k + 2$ nodal intervals. These one-dimensional basis functions, as well as multidimensional ones obtained as a tensor product of the one-dimensional splines, represent a partition of unity with unit coefficients:

$$\sum_{i\in\Omega} X_i(\mathbf{x}) \equiv 1, \quad \mathbf{x} \in [0,1]^3. \tag{18}$$

Fig. 3 shows an example of one-dimensional cubic splines with defect one built over an interval $[0,1]$ with seven uniform subdivisions.

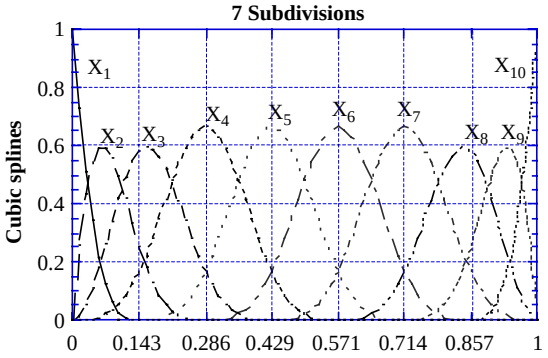

Fig. 3. Overlapping cubic B-spline functions with seven subdivisions.

3.2. B-spline approximation in arbitrary volumes

The approximation in Eq. (17) was applied piecewise to volume partitions of the structure of interest, so that each of the partitions can be conformably mapped onto the unit volume $[0,1]^3$. In the case of B-spline approximation, the boundaries between these regions are the only surfaces of C^0 displacement continuity. Inside these volumes, the displacement approximation smoothness is defined by the defect of the spline approximation. It is therefore desired to have large and few partitions with the B-spline approximation, while, in the case of the p-type approximation, a given accuracy can be achieved only by increasing the power of approximation after the elements are defined.

In the present case, a natural subdivision for the unit-cell of the woven composite would be the volumes occupied by yarns and the matrix. Thus the displacement and stress continuity within each yarn and matrix volume is assured by using low defect spline approximation, while the C^0 continuity between them reflects that occurring on the material interface. The 3-D displacement approximation is written as

$$\mathbf{u}(\mathbf{x}) = \sum_{i\in\Omega_j} X_i(\boldsymbol{\varsigma})\mathbf{U}_i, \quad \mathbf{x} = \boldsymbol{\eta}_i(\boldsymbol{\varsigma}),\ j = 1,\ldots,6, \tag{19}$$

where the entire volume of the unit-cell is divided into six subvolumes, as shown in Fig. 2. The sets of indexes Ω_j, $j = 1,\ldots,6$ in each subvolume depend upon the type of spline subdivision density utilized. Curvilinear transformations $\mathbf{x} = \boldsymbol{\eta}_i(\boldsymbol{\varsigma})$ were defined in each subvolume to map their physical volume into the unit volume. Here and below we shall use the variable, $\boldsymbol{\varsigma}$, $\boldsymbol{\varsigma} \in [0,1]^3$ to designate the local coordinates of a point in each subvolume and $\mathbf{x}$ to designate its global *xyz*-coordinates. The approximation in Eq. (19) satisfies the partition of unity feature since it is granted on each subvolume by Eq. (18).

Consider a delamination between yarns (subvolumes) 1 and 2 along the boundary 3, as shown in Fig. 2. The curvilinear geometry of the unit-cell requires an application of the contact algorithm in order to model the yarn delamination damage mode and prevent interpenetration, which may occur between the delamination surfaces under specified loading conditions. A penalty function approach along with contact surface characteristic functions was used to formulate the contact problem.

We shall designate the surface of the delamination as Γ_c at which either full or partial separation of the yarns takes place. We choose yarn 1 as a controlling one in the contact formulation and all geometric parameters are expressed in its coordinates. A non-penetration condition is expressed with unit vectors that are normal, $\mathbf{n}(\mathbf{x})$, and tangential, $\mathbf{t}_1(\mathbf{x})$ and $\mathbf{t}_2(\mathbf{x})$, to the contact surface, Γ_c, where $\mathbf{x} = \boldsymbol{\eta}_1(\boldsymbol{\varsigma})$ are the global coordinates of the points on the contact surface of yarn 1 before deformation. The following conditions will assure the non-penetration:

$$[\mathbf{u}^{(1)}(\mathbf{x}) - \mathbf{u}^{(2)}(\mathbf{x})]\mathbf{n}(\mathbf{x}) \leqslant 0, \tag{20}$$

where $\mathbf{u}^{(1)}$ and $\mathbf{u}^{(2)}$ are displacement vectors of yarns 1 and 2, respectively. The tangential alignment conditions are *a priori* satisfied in the infinitesimal limit, since the displacement jump on the surface of delamination under zero loading is assumed not to exist. This simplification allows straightforward variational formulation of the contact problem, which is based on minimization of the following functional constructed by using penalty function formulation and contact surface characteristic function $H(\mathbf{x})$:

$$L = W(\mathbf{u}) - \int\int_{S_t} \mathbf{T}\mathbf{u}\,\mathrm{d}s + \alpha \int\int_{\Gamma_c} H(\mathbf{x})\left\{[\mathbf{u}^{(1)}(\mathbf{x}) - \mathbf{u}^{(2)}(\mathbf{x})]\mathbf{n}(\mathbf{x})\right\}^2 \mathrm{d}s, \tag{21}$$

where $W(\mathbf{u})$ is the total strain energy density function for the entire unit-cell, calculated by excluding the delamination surface, α is the penalty parameter and S_t is the traction-loaded portion of the outer boundary of the unit-cell, not containing the contact surface.

The characteristic function H, which is unity in the contact surface and zero elsewhere, can also be approximated by using the spline functions. A subset $\omega_c \in \Omega_1$ of the displacement approximation functions of yarn 1 is defined by selecting the functions that are nonzeros anywhere on the surface Γ_c. This subset also forms a partition of unity approximation, but only at the contact surface. Consider a set of binary coefficients h_i, $i \in \omega_c$, which can only be equal to 1 or 0. The following approximation for the characteristic function on the surface Γ_c is defined as

$$H(\mathbf{x}) \equiv \sum_{i\in\omega_c} h_i X_i(\boldsymbol{\varsigma}), \quad \mathbf{x} = \boldsymbol{\eta}_1(\boldsymbol{\varsigma}). \tag{22}$$

The contact surface characteristic function H is found iteratively by increasing the contact zone by setting $h_i = 1$ if

$$\int\int_{\Gamma_c} [\mathbf{u}^{(1)}(\mathbf{x}) - \mathbf{u}^{(2)}(\mathbf{x})]\mathbf{n}(\mathbf{x}) X_i\,\mathrm{d}s > 0, \tag{23}$$

which indicates penetration, and reducing the contact zone by setting $h_i = 0$ if

$$\int\int_{\Gamma_c} H(\mathbf{x})[\mathbf{u}^{(1)}(\mathbf{x}) - \mathbf{u}^{(2)}(\mathbf{x})]\mathbf{n}(\mathbf{x}) X_i\,\mathrm{d}s < 0, \tag{24}$$

which indicates the presence of separation in the region of nonzero contact tractions.

4. Numerical results

The displacement and stress fields in the yarn and matrix must satisfy interfacial continuity conditions. The continuity of the displacements is assured due to the nature of the approximation method, while the inter-yarn traction continuity conditions can only be satisfied in the limit of mesh refinement. We shall examine these continuity conditions on the yarn–yarn and yarn–matrix interfaces along lines 1, 2 and 3, which are drawn with double lines in Fig. 2. The stresses will be shown in the local $\hat{x}_1\hat{x}_2\hat{x}_3$ coordinate systems such that the $\hat{x}_3$-axis is normal to the undulated surface under consideration. The displacement and stress fields in these coordinates are denoted as $\hat{u}$ and $\hat{\sigma}$, and are obtained from those in the global *xyz*-coordinates by using the following transformations:

$$\{\hat{u}\} = [L_2(\theta_2)]^{-1}\{u\}_{\text{global}}, \tag{25}$$

$$\{\hat{\sigma}\} = [T_2(\theta_2)]^{-1}\{\sigma\}_{\text{global}}, \tag{26}$$

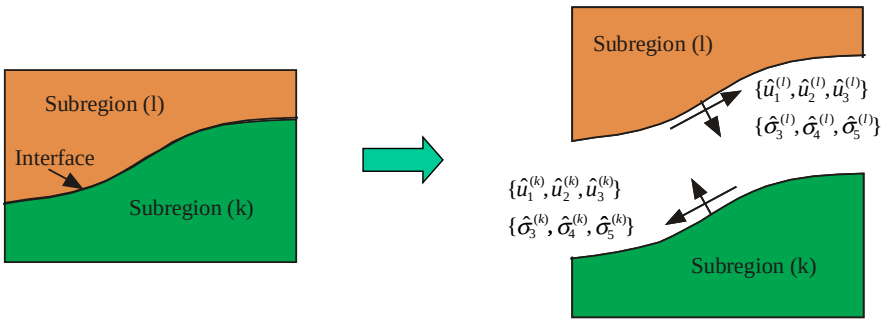

Fig. 4. Displacement and traction continuity conditions at the interface between subregions (k) and (l).

where $[L_2(\theta_2)]^{-1} = [L_2(-\theta_2)]$ and $[T_2(\theta_2)]^{-1} = [T_2(-\theta_2)]$. As Fig. 4 shows, the interface continuity conditions are satisfied if

$$\begin{cases} \widehat{u}_1^{(k)} = \widehat{u}_1^{(l)}, \\ \widehat{u}_2^{(k)} = \widehat{u}_2^{(l)}, \\ \widehat{u}_3^{(k)} = \widehat{u}_3^{(l)}, \end{cases} \tag{27}$$

$$\begin{cases} \widehat{\sigma}_3^{(k)} = \widehat{\sigma}_3^{(l)}, \\ \widehat{\sigma}_4^{(k)} = \widehat{\sigma}_4^{(l)}, \\ \widehat{\sigma}_5^{(k)} = \widehat{\sigma}_5^{(l)}, \end{cases} \tag{28}$$

where contracted notations are used for the stress components so that $\widehat{\sigma}_1$, $\widehat{\sigma}_2$, $\widehat{\sigma}_3$, $\widehat{\sigma}_4$, $\widehat{\sigma}_5$, $\widehat{\sigma}_6$ correspond to $\widehat{\sigma}_{11}$, $\widehat{\sigma}_{22}$, $\widehat{\sigma}_{33}$, $\widehat{\sigma}_{23}$, $\widehat{\sigma}_{13}$, $\widehat{\sigma}_{12}$, respectively. Note that $\widehat{\sigma}_3$ is the interfacial normal stress, and $\widehat{\sigma}_4$ and $\widehat{\sigma}_5$ are the interfacial shear stress components. The subscripts (k) and (l) denote the subregion numbers.

The interfacial normal and shear stress fields were calculated along three inter-yarn boundaries taken at the $y = 0$ face of the unit-cell. These three inter-yarn boundaries between (1) bottom matrix and warp yarn (subregions 5 and 1), (2) bottom matrix and fill yarn (subregions 5 and 2) and (3) fill and warp yarns (subregions 2 and 1) are shown in Fig. 2 by double lines. The results for $\widehat{\sigma}_4$ are not shown here since they are negligible under the applied loading condition.

By using Eq. (4), the crimp angles (θ_2) along the inter-yarn boundaries were calculated from the derivatives of the lower or upper surface functions in Eqs. (1), so that the crimp angles along interface lines 1 and 3 were calculated with $z_L^{(1)}$ of the subregion 1, and along interface line 2 with $z_L^{(2)}$ of the subregion 2. For example, the crimp angle along interface line 3 can be obtained as

$$\theta_2(x, y = 0) = -\tan^{-1}\left(\frac{\partial z_L^{(1)}}{\partial x}\right)\bigg|_{y=0} = -\tan^{-1}\left(\frac{\pi t_f}{L_w}\sin\left(\frac{\pi x}{L_w}\right)\right), \tag{29}$$

and is plotted in Fig. 5. Note that $\theta_2(x = L_w/2, y = 0) = -\tan^{-1}(\pi t_f/L_w) = -8.927°$.

Figs. 6–11 show the interfacial normal ($\widehat{\sigma}_3$) and shear stress ($\widehat{\sigma}_5$) distributions calculated with three different mesh schemes along the inter-yarn boundaries. Numbers in circles are the interface numbers. Triangular and circular markers indicate the stress fields in upper (z^+) and lower (z^-) subregions, respectively. The interfacial stress continuity conditions are satisfied when two lines with triangular and circular markers coincide with each other. Quadratic spline functions were used for the displacement approximation in all directions.

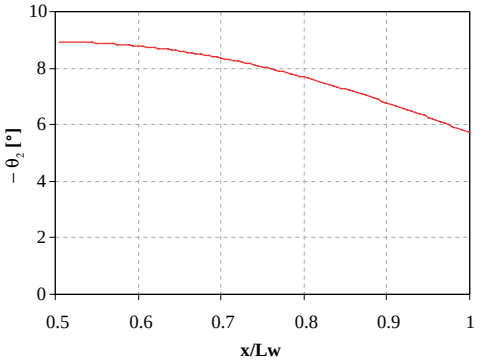

Fig. 5. A distribution of yarn crimp angles along interface line 3 in Fig. 2.

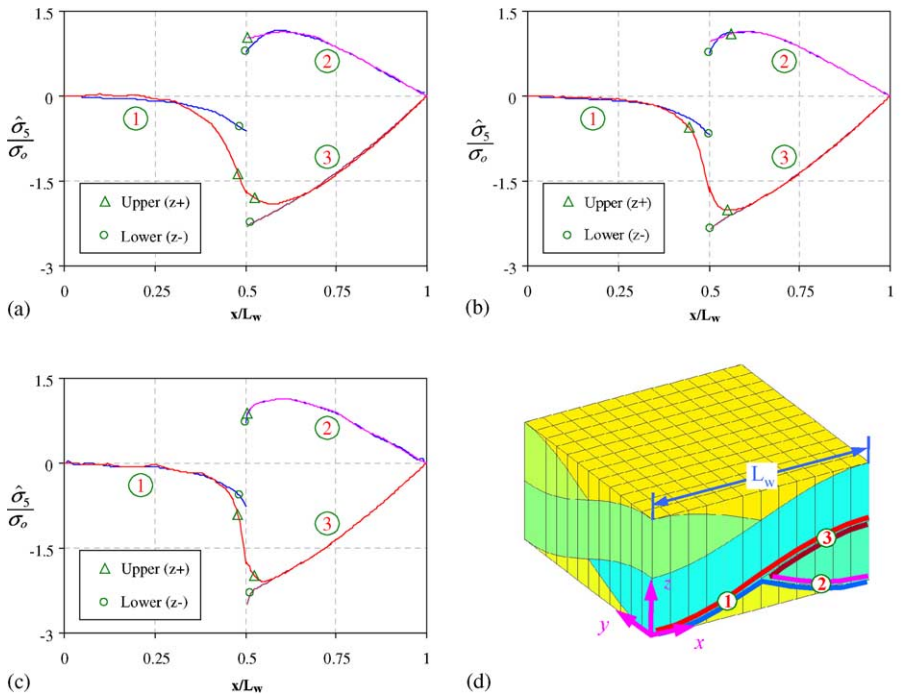

Fig. 6. Interfacial shear stress ($\widehat{\sigma}_5$) distributions on a unit-cell of undamaged woven composites along three inter-yarn boundaries calculated with three different mesh schemes. Numbers in circles are interface line numbers: (a) $\widehat{\sigma}_5$ with mesh #1, (b) $\widehat{\sigma}_5$ with mesh #2, (c) $\widehat{\sigma}_5$ with mesh #3, (d) interface lines in a unit-cell.

Fig. 6 shows the interfacial shear stress ($\widehat{\sigma}_5$) distributions along the three inter-yarn boundaries on lines 1, 2 and 3. The inter-yarn shear stress distributions exhibit visible discontinuity between the upper and lower surfaces on interfaces 1, 2 and 3 with the considered mesh refinements. With the coarsest mesh #1, the stress continuity condition is not satisfied within approximately $0.3 < x/L_w < 0.65$. Note that the thickness of the fill yarn (subregion 2) is zero at $x = L_w/2$. The upper-surface stress components on interfaces 1 and 3 form a continuous curve, since the upper surfaces of interfaces 1 and 3 form continuous lower surfaces of the warp yarn (subregion 1). However, unlike the upper-surface components on interfaces 1 and 3, the

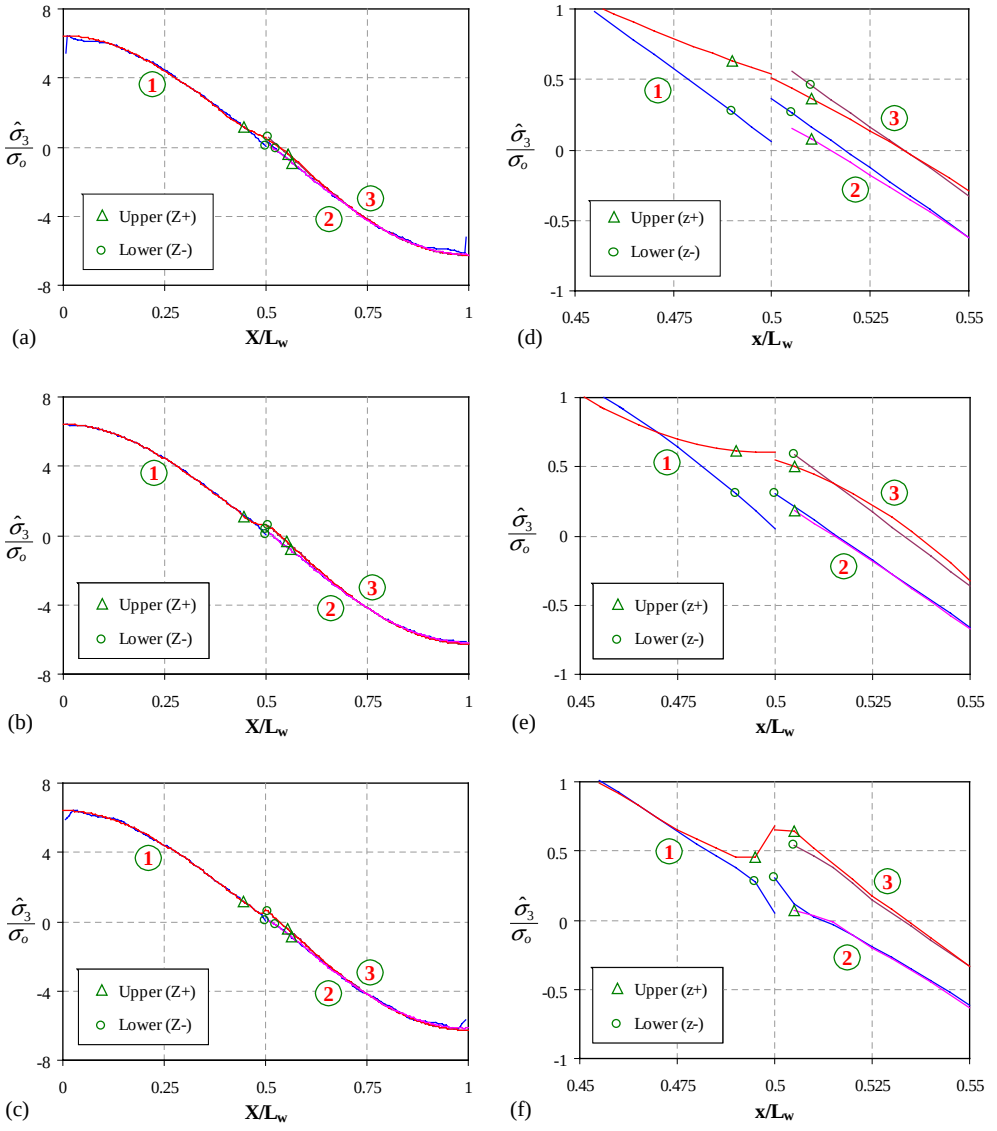

Fig. 7. Interfacial normal stress ($\hat{\sigma}_3$) distributions on a unit-cell of undamaged woven composites along three inter-yarn boundaries calculated with three different mesh schemes. Numbers in circles are interface line numbers: (a)–(c) for $0 < x/L_w < 1$ and (d)–(f) for $0.45 < x/L_w < 0.55$. (a) $\hat{\sigma}_3$ with mesh #1 ($0 < x/L_w < 1$), (b) $\hat{\sigma}_3$ with mesh #2 ($0 < x/L_w < 1$), (c) $\hat{\sigma}_3$ with mesh #3 ($0 < x/L_w < 1$), (d) $\hat{\sigma}_3$ with mesh #1 ($0.45 < x/L_w < 0.55$), (e) $\hat{\sigma}_3$ with mesh #2 ($0.45 < x/L_w < 0.55$), (f) $\hat{\sigma}_3$ with mesh #3 ($0.45 < x/L_w < 0.55$).

lower-surface shear stresses on these interfaces yielded a significant stress jump at $x = L_w/2$. Because of the presence of interface 2, the lower-surface components on interfaces 1 and 3 became significantly influenced by the stress components on interface 2 at the point $x = L_w/2$, and thus yielded a directionally nonunique stress field, causing the stress singularity (Iarve and Pagano, 2001). Since the continuity conditions were not satisfied, the accuracy of the stress solution became questionable. With the mesh refinement, the region of the inter-yarn shear stress discontinuity is reduced to approximately $0.4 < x/L_w < 0.6$ with mesh #2 and

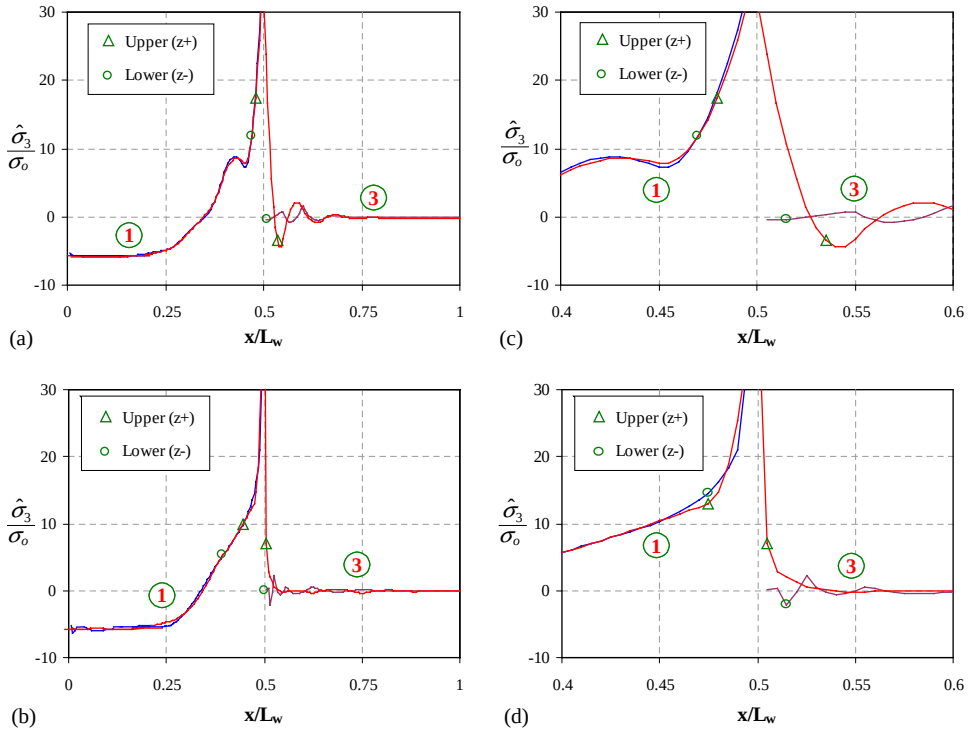

Fig. 8. Interfacial normal stress ($\widehat{\sigma}_3$) distributions on a unit-cell of damaged woven composites in a crack-opening mode under a compressive loading along two inter-yarn boundaries calculated with two different mesh schemes. Numbers in circles are interface line numbers. (a) and (b) for $0 < x/L_w < 1$ and (c) and (d) for $0.4 < x/L_w < 0.5$. (a) $\widehat{\sigma}_3$ with mesh #2 ($0 < x/L_w < 1$), (b) $\widehat{\sigma}_3$ with mesh #3 ($0 < x/L_w < 1$), (c) $\widehat{\sigma}_3$ with mesh #2 ($0.4 < x/L_w < 0.5$), (d) $\widehat{\sigma}_3$ with mesh #3 ($0.4 < x/L_w < 0.5$).

$0.45 < x/L_w < 0.55$ with mesh #3, as shown in Figs. 6(b) and (c), respectively. However, the accuracy of the stress prediction in the vicinity of the stress singularity is a well-known shortcoming of polynomial approximation based methods (Iarve and Pagano, 2001), and needs to be addressed by using a local asymptotic solution.

Fig. 7 shows the interfacial shear stress ($\widehat{\sigma}_5$) distributions along the three inter-yarn boundaries on lines 1, 2 and 3. Figs. 7(a)–(c), which are plotted for $0 < x/L_w < 1$, were zoomed in toward the singular point and plotted for $0.45 < x/L_w < 0.55$ in Figs. 7(d)–(f). The results shown in Figs. 7(a)–(c) indicate that the numerical values of the inter-yarn normal stress did not exhibit trends typical for unbounded stress behavior, and this stress component appeared to satisfy the traction continuity conditions at the yarn–yarn and the yarn–matrix interfaces and pass continuously through the singular point. However, the zoomed figures in Figs. 7(d)–(f) within $0.45 < x/L_w < 0.55$ clearly shows the inter-yarn normal stress distributions exhibit visible discontinuity between the upper and lower surfaces on interfaces 1, 2 and 3 in the vicinity of the singular point. Note that the discontinuity also appeared near $x = 0$ and $x = L_w$, where the matrix subregion has zero thickness. The singularity is due to the artificial zero thickness matrix subregion and can be eliminated by incorporating more realistic geometry in the unit-cell. Therefore, this problem will not be treated in this study.

Consider delamination between the warp yarn (subregion 1) and the fill yarn (subregion 2) along interface line 3. The continuity boundary conditions of displacement and stress components in Eqs. (27) and (28) are no longer valid on this delaminated surface. The boundary conditions with the damaged

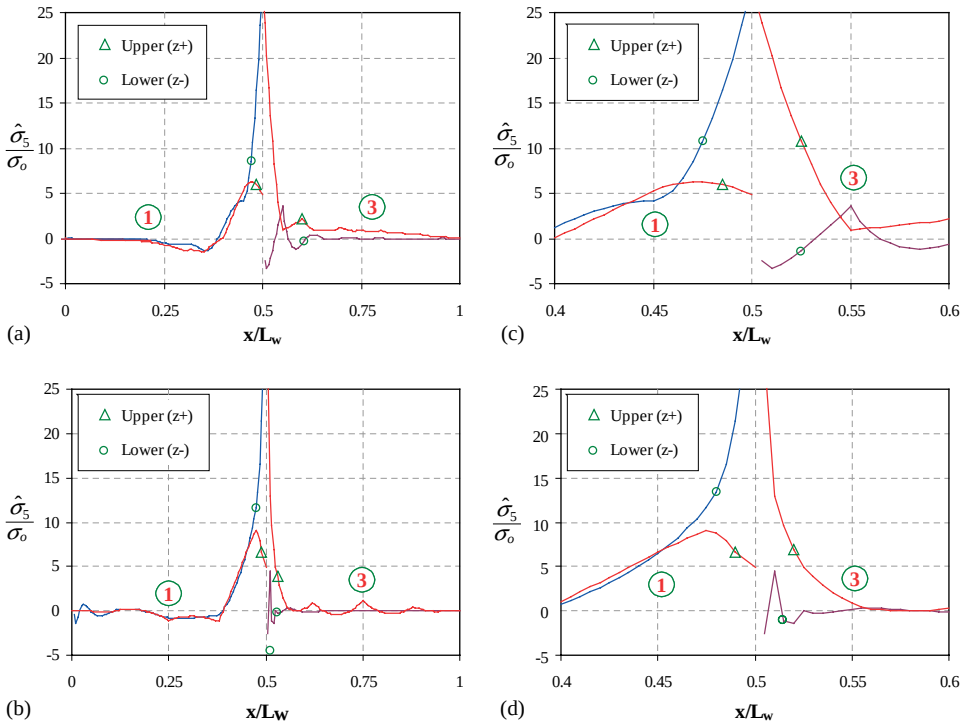

Fig. 9. Interfacial shear stress ($\widehat{\sigma}_5$) distributions on a unit-cell of damaged woven composites in a crack-opening mode under a compressive loading along two inter-yarn boundaries calculated with two different mesh schemes. Numbers in circles are interface line numbers. (a) and (b) for $0 < x/L_w < 1$ and (c) and (d) for $0.4 < x/L_w < 0.5$. (a) $\widehat{\sigma}_5$ with mesh #2 ($0 < x/L_w < 1$), (b) $\widehat{\sigma}_5$ with mesh #3 ($0 < x/L_w < 1$), (c) $\widehat{\sigma}_5$ with mesh #2 ($0.4 < x/L_w < 0.5$), (d) $\widehat{\sigma}_5$ with mesh #3 ($0.4 < x/L_w < 0.5$).

unit-cell are dependent on the applied loading conditions. For example, if a compressive load is applied with $u_o < 0$ in Eq. (16), the damaged surfaces are in an opening crack mode, and the corresponding inter-yarn boundary conditions on the crack surfaces are written as

$$\begin{cases} \widehat{\sigma}_3^{(k)} = \widehat{\sigma}_3^{(l)} = 0, \\ \widehat{\sigma}_4^{(k)} = \widehat{\sigma}_4^{(l)} = 0, \\ \widehat{\sigma}_5^{(k)} = \widehat{\sigma}_5^{(l)} = 0. \end{cases} \tag{30}$$

Meanwhile, if the tensile load is applied with $u_o > 0$, the damaged surfaces are in a closing crack mode so that they are in contact with each other, and the corresponding inter-yarn boundary conditions on the contacted surfaces with a frictionless assumption are written as

$$\begin{cases} \widehat{u}_3^{(k)} = \widehat{u}_3^{(l)}, \\ \widehat{\sigma}_3^{(k)} = \widehat{\sigma}_3^{(l)}, \\ \widehat{\sigma}_4^{(k)} = \widehat{\sigma}_4^{(l)} = 0, \\ \widehat{\sigma}_5^{(k)} = \widehat{\sigma}_5^{(l)} = 0. \end{cases} \tag{31}$$

The interfacial normal ($\widehat{\sigma}_3$) and shear stress ($\widehat{\sigma}_5$) distributions along interface lines 1 and 3 in the presence of the delamination on line 3 are shown in Figs. 8 and 9 for the crack opening case and Figs. 10 and 11 for

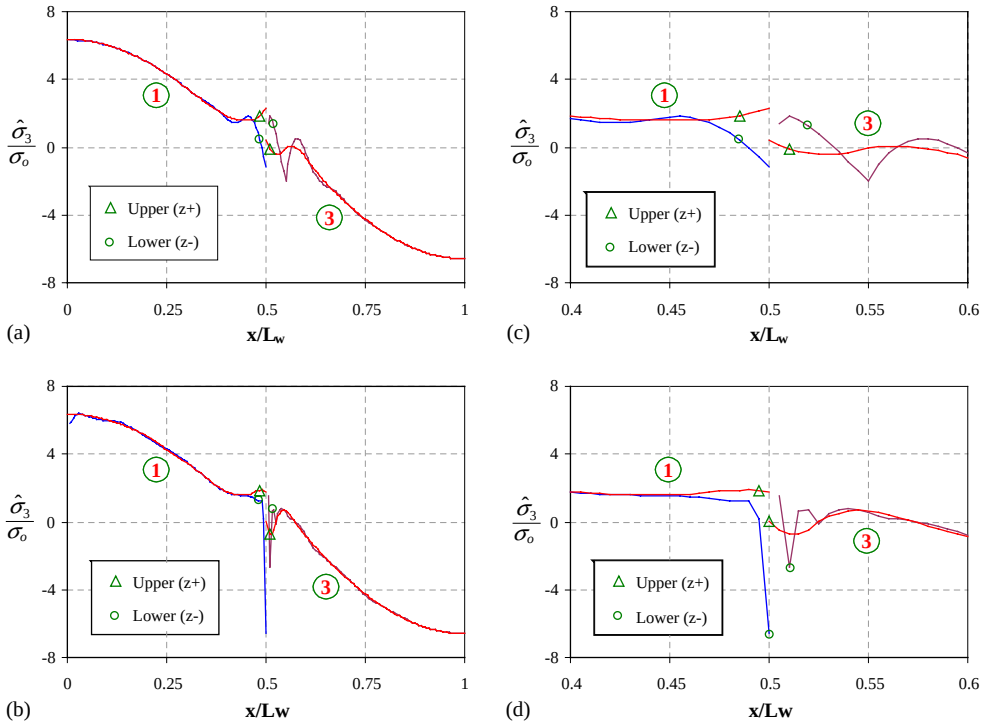

Fig. 10. Interfacial normal stress ($\hat{\sigma}_3$) distributions on a unit-cell of damaged woven composites in a crack-closing mode under a tensile loading along two inter-yarn boundaries calculated with two different mesh schemes. Numbers in circles are interface line numbers. (a) and (b) for $0 < x/L_w < 1$ and (c) and (d) for $0.4 < x/L_w < 0.5$. (a) $\hat{\sigma}_3$ with mesh #2 ($0 < x/L_w < 1$), (b) $\hat{\sigma}_3$ with mesh #3 ($0 < x/L_w < 1$), (c) $\hat{\sigma}_3$ with mesh #2 ($0.4 < x/L_w < 0.5$), (d) $\hat{\sigma}_3$ with mesh #3 ($0.4 < x/L_w < 0.5$).

the crack closing (contact) modes. Calculations with the refined meshes #2 and #3 only were shown here, and those with the coarse mesh #1 were omitted. The result on interface line 2 is also omitted. Figs. 8–11(a)–(b), which are plotted for $0 < x/L_w < 1$, were zoomed in toward the singular point and plotted for $0.4 < x/L_w < 0.5$ in Figs. 8–11(c)–(d). The interfacial stress continuity conditions in Eq. (28) must still be satisfied on interface line 1, while the crack-opening or the contact boundary conditions in Eqs. (30) and (31) must be satisfied on interface line 3. Mesh refinement has reduced the inter-yarn stress discontinuity region for both crack configurations.

As Figs. 8–11 show, the normal and shear stress components on interface 3 exhibit singular behavior near the singular point $x = L_w/2$. While the crack surfaces enforce the stress-free boundary conditions on the upper side of interface 3, the continuity boundary conditions require smooth transition of the upper-side stress components between interfaces 1 and 3. Therefore, unless the stress on the upper-side of interface 1 is zero, the stress-free and continuity boundary conditions are contradictory to each other. The non-uniqueness of the stress values in the vicinity of the singular point cannot be captured by using the polynomial displacement approximation functions. Because of the high stress concentration, the inter-yarn stress discontinuity between the upper- and lower-surfaces is more significant than that in the undamaged case in Figs. 6 and 7. In the presence of delamination, even the inter-yarn normal stress exhibits the visible unbounded stress behavior and is discontinuous across the inter-yarn boundaries in the vicinity of $x = L_w/2$ in both open- and the closed-crack cases.

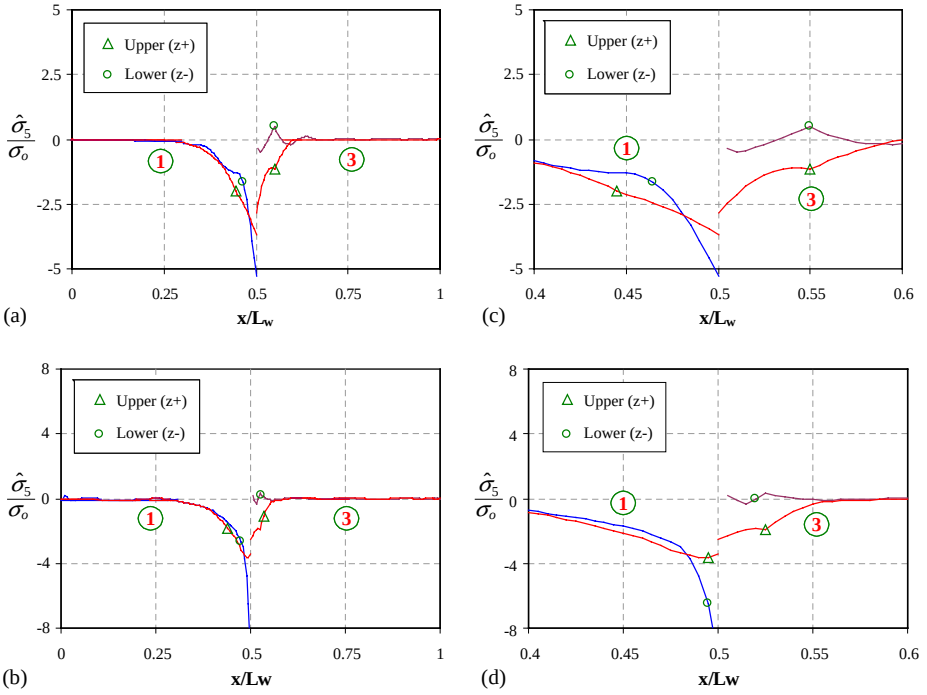

Fig. 11. Interfacial shear stress ($\hat{\sigma}_5$) distributions on a unit-cell of damaged woven composites in a crack-closing mode under a tensile loading along two inter-yarn boundaries calculated with two different mesh schemes. Numbers in circles are interface line numbers. (a) and (b) for $0 < x/L_w < 1$ and (c) and (d) for $0.4 < x/L_w < 0.5$. (a) $\hat{\sigma}_5$ with mesh #2 ($0 < x/L_w < 1$), (b) $\hat{\sigma}_5$ with mesh #3 ($0 < x/L_w < 1$), (c) $\hat{\sigma}_5$ with mesh #2 ($0.4 < x/L_w < 0.5$), (d) $\hat{\sigma}_5$ with mesh #3 ($0.4 < x/L_w < 0.5$).

5. Summary and conclusions

The unit-cell of the plain-woven composite was modeled and analyzed with the 3-D numerical analysis based on B-spline displacement approximation functions. The model calculated the 3-D stress field in the woven composites with and without delamination damage at the yarn interface. The unit-cell model was divided into several homogeneous subregions; each subregion was occupied by a characteristic fabric yarn or matrix. The spline approximation provides continuity of displacement and stress components within each yarn and matrix subregion. The penalty function method along with the contact surface characteristic function was used to obtain the full-field numerical solution for the frictionless contact problem between delaminated yarn surfaces.

Stress distributions in the unit-cells with perfect bonding between the yarn interfaces were obtained with various mesh densities. The numerical values of the inter-yarn normal stress did not exhibit trends typical for unbounded stress behavior. This stress component appeared to satisfy the traction continuity conditions at the yarn–yarn and the yarn–matrix interfaces and pass continuously through the singular point. The inter-yarn shear stress components, on the other hand, displayed discontinuous behavior typical for numerical results in the vicinity of the stress singularity. In the presence of delamination, both the inter-yarn normal and shear stress components exhibited unbounded behavior near the singularity. Notably, the inter-yarn normal stress shows signs of singular behavior in both cases of open- and closed-delaminations.

Due to the stress singularity that exists at yarn-crossover locations containing three materials (yarn–yarn–matrix) interface intersections, the full-field numerical solution, even with high-order approximation

functions, found to be unable to capture the directional nonuniqueness of the stress values in the vicinity of the singularity, and thus did not provide accurate prediction of the stress components. Therefore, it is essential to incorporate analysis methods to capture the singular behavior at the singular points, such as an asymptotic singular stress analysis, which will be given in a follow-on paper (Sihn et al., accepted for publication).

References

BSAM User's Manual, 2003, University of Dayton Research Institute.

Bystrom, J., Jekabsons, N., Varna, J., 2000. An evaluation of different models for prediction of elastic properties of woven composites. Composites Part B 31 (1), 7–20.

Drapier, S., Wisnom, M.R., 1999. A finite-element investigation of the interlaminar shear behaviour of non-crimp-fabric-based composites. Composite Science and Technology 39, 2351–2362.

Iarve, E.V., 1996. Spline variational three-dimensional stress analysis of laminated composite plates with open holes. International Journal of Solids and Structures 44 (14), 2095–2118.

Iarve, E.V., 1997. Three-dimensional stress analysis in laminated composites with fasteners based on the B-spline approximation. Composites Part A 28A, 559–571.

Iarve, E.V., Pagano, N.J., 2001. Singular full-field stresses in composite laminates with open holes. International Journal of Solids and Structures 38 (1), 1–28.

Naik, N.K., Ganesh, V.K., 1992. Prediction of on-axes elastic properties of plain weave fabric composites. Composite Science and Technology 45 (2), 135–152.

Naik, N.K., Ganesh, V.K., 1994. Failure behavior of plain weave fabric laminates under in-plane shear loading. Journal of Composites Technology & Research 16 (1), 3–20.

Naik, N.K., Ganesh, V.K., 1996. Failure behavior of plain weave fabric laminates under on-axis uniaxial tensile loading: II. Analytical predictions. Journal of Composite Materials 30 (16), 1779–1822.

Naik, N.K., Shembekar, P.S., 1992. Elastic behavior of woven fabric composites: I. Lamina analysis. Journal of Composite Materials 26 (15), 2197–2225.

Naik, N.K., Azad, S.K.N.M., Prasad, P.D., 2002. Stress and failure analysis of 3D angle interlock woven composites. Journal of Composite Materials 36 (1), 93–123.

Roy, A.K., 1996. In situ damage observation and failure in model laminates containing planar yarn crimping of woven composites. Mechanics of Composite Materials and Structures 3, 101–117.

Shembekar, P.S., Naik, N.K., 1992. Elastic behavior of woven fabric composites: II. Laminate analysis. Journal of Composite Materials 26 (15), 2226–2246.

Sihn, S., Roy, A.K., 2001. Development of a three-dimensional mixed variational model for woven composites: Part II. Numerical solution and validation. International Journal of Solids and Structures 38 (34–35), 5949–5962.

Sihn, S., Iarve, E.V., Roy, A.K., accepted for publication. Three-dimensional stress analysis of textile woven composites: Part II. Asymptotic analysis, International Journal of Solids and Structures.

Tan, P., Tong, L., Steven, G.P., 1997. Modeling for predicting the mechanical properties of textile composites: a review. Composites Part A 28A, 903–922.

Whitcomb, J.D., 1991. Three-dimensional stress analysis of plain weave composites. In: O'Brien, T.K. (Ed.), Composite Materials: Fatigue and Fracture. In: ASTM STP 1110, 3. American Society for Testing and Materials, Philadelphia, pp. 417–438.

Woo, K., Whitcomb, J.D., 1994. Global/local finite element analysis for textile composites. Journal of Composite Materials 28 (14), 1305–1321.

Woo, K., Whitcomb, J.D., 1996. Three-dimensional failure analysis of plain weave textile composites using a global/local finite element method. Journal of Composite Materials 30 (9), 948–1003.

Woo, K., Whitcomb, J.D., 2000. A post-processor approach for stress analysis of woven textile composites. Composites Science and Technology 60 (5), 693–704.

Tsai, S.W., 1992. Theory of Composites Design. Think Composites, Dayton, OH.

Yang, J.M., Ma, C.L., Chou, T.-W., 1986. Fiber inclination model of three-dimensional textile structural composites. Journal of Composite Materials 20 (5), 472–483.